Science of the Total Environment 613–614 (2018) 1417–1429

Contents lists available at ScienceDirect

Science of the Total Environment

journal homepage: www.elsevier.com/locate/scitotenv

Assessing the impacts of urban sprawl on net primary productivity using fusion of Landsat and MODIS data

Yuchao Yan, Xiaoping Liu *, Feiyue Wang, Xia Li, Jinpei Ou, Youyue Wen, Xun Liang

Guangdong Key Laboratory for Urbanization and Geo-simulation, School of Geography and Planning, Sun Yat-sen University, Guangzhou 510275, PR China

HIGHLIGHTS

- Quantifying the impacts of urban sprawl on NPP at a fine resolution
- The accuracy of NPP was improved using spatiotemporal fusion algorithm.
- The loss in 30-m resolution NPP was much higher than 500-m resolution NPP.

GRAPHICAL ABSTRACT

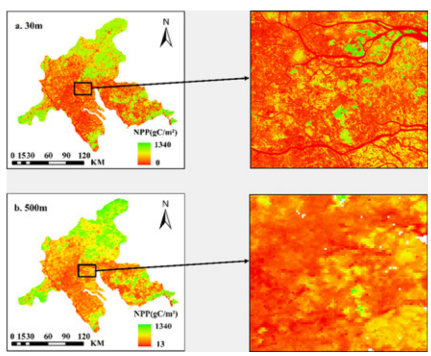

ARTICLE INFO

Article history:
Received 8 April 2017
Received in revised form 13 September 2017
Accepted 14 September 2017
Available online 12 October 2017

Editor: D. Barcelo

Keywords:
Urban sprawl
NPP
CASA model
Spatiotemporal fusion algorithm
FLUS model

ABSTRACT

Urbanization has profoundly altered the terrestrial ecosystem carbon cycle, especially the net primary productivity (NPP). Many attempts have been made to assess the influence of urbanization on NPP at coarse resolutions (e.g., 250 m or larger), which may ignore many smaller and highly fragmented urban lands, and to a large extent, underestimate the NPP variations induced by urban sprawl. Hence, we attempted to analyze the NPP variations influenced by urban sprawl at a fine resolution (e.g., 30 m), toward which the accuracy of NPP was improved using remotely sensed data fusion algorithm. In this paper, this assumption was tested in the Pearl River Delta of China. The land cover datasets from the Landsat Thematic Mapper (TM)/Enhanced Thematic Mapper Plus (ETM+) were acquired to quantify the urban sprawl. The synthetic Normal Differential Vegetation Index (NDVI) data was obtained by fusing Landsat and Moderate Resolution Imaging Spectroradiometer (MODIS) NDVI via spatiotemporal fusion algorithm. The Carnegie-Ames-Stanford Approach (CASA) model was driven by land cover map, synthetic NDVI and meteorological data to estimate the 30-m resolution NPP. Then, we analyzed the influence of urban sprawl on 30-m resolution NPP during the period of 2001–2009. Additionally, we also simulated the spatiotemporal change of future urban sprawl under different scenarios using the Future Land Use Simulation (FLUS) model, and further analyzed its influence on 30-m resolution NPP. Our results showed that the accuracy of 30-m resolution NPP from synthetic NDVI is better than 500-m resolution NPP from MODIS NDVI. The loss in 30-m resolution NPP due to urban sprawl was much higher than 500-m resolution NPP. Moreover, the harmonious development scenario, characterized by a reasonable size of urban sprawl and a corresponding lower NPP loss from 2009 to 2050, would be considered as a more human-oriented and sustainable development strategy.

1. Introduction

Land-use/cover change (LUCC) has become an important field of global change research since the 1990s (Prentice and Fung, 1990;

* Corresponding author.
E-mail address: liuxp3@mail.sysu.edu.cn (X. Liu).

https://doi.org/10.1016/j.scitotenv.2017.09.139

Canadell and Mooney, 1999). As one of the most extreme anthropogenic LUCC, the process of urbanization associated with urban sprawl, population growth and economic development, was expected to continue to strengthen worldwide (Grimm et al., 2008; Lu et al., 2010; Buyantuyev et al., 2010). Urban sprawl involving the conversion of high productive forestland and fertile cropland to urban land, not only decreases the carbon sequestration potential of vegetation and soil, but also creates a threat to natural resources and food security (Nizeyimana et al., 2001; Shochat et al., 2006; Xu et al., 2007; Grimm et al., 2008). What's worse, the urban development consumes enormous amounts of fossil fuels to meet the growth demands of industrial manufacture and people's life, resulting in large quantities of greenhouse gases into the atmosphere (Wise et al., 2010). It was estimated that approximately 97% of anthropogenic CO_2 emissions originated from urban areas (Svirejeva-Hopkins et al., 2004). As a result, urbanization dramatically alters the composition, structure and function of the ecosystem, and further greatly influences the global carbon cycle and climate change (Defries et al., 1999; Trenberth et al., 2007).

As a significant component of the carbon cycle, NPP represents the amount of dry organic matter accumulated by vegetation per unit area and per unit time through the process of photosynthesis, and directly reflects the productivity of vegetation under the natural environmental conditions (Lieth and Whittaker, 1975; Oke et al., 1989; Field et al., 1998). It's worth noting that NPP acts not only as the driving force of the carbon cycle, but also as a primary factor to investigate the carbon source and sink, and to adjust the ecosystem processes (Field et al., 1998). Thus, it can be used as a "common currency" for assessing the influence of urbanization on the ecological environment (Imhoff et al., 2004; Xu et al., 2007).

Some studies have been published considering how urbanization impacts on NPP ranging from the regional to the national scale, where the NPP was often estimated using the parametric or process models coupled with remotely sensed data. Imhoff et al. (2004) evaluated the consequences of urbanization on NPP in the United States and estimated the NPP using AVHRR data as the input to the CASA model. Buyantuyev and Wu (2009) analyzed how urbanization altered the spatiotemporal patterns of NPP in the Phoenix, USA. In this research, a simplified parametric NPP model was calculated using MODIS NDVI data. Wu et al. (2014) identified the contribution of urbanization to NPP variations in the Yangtze River Delta of China and calculated the NPP using 10-day SPOT VEGETATION NDVI images. Tian and Qiao (2014) assessed the influence of urbanization on NPP in China, using NPP as a product of the GLO-PEM model driven by AVHRR data. Furthermore, Pei et al. (2013) also explored the differences in NPP between pre- and post-urban development in China, and the NPP resulting from CASA model driven by MODIS NDVI data. In these studies, NPP was estimated at coarse resolutions (250 m–1000 m), which was appropriate for quantifying how urban sprawl affected NPP at large spatial scales, but might result in the NPP variations induced by urban sprawl being underestimated at fine spatial scales, because the highly fragmented and heterogeneous landscapes in urban areas shaped by environmental processes and socio-economic drivers limit the access to information on vegetation structure and dynamics (Buyantuyev and Wu, 2009). Nevertheless, at present, only a few studies focus on investigating the influence of urban sprawl on NPP at a fine resolution. In addition, most prior researches have studied the consequences of past urban sprawl on NPP, but little is known about NPP variations under the influence of future urban sprawl at a fine resolution.

To evaluate the influence of urban sprawl on NPP accurately, it is crucial to found a way to improve the accuracy of NPP estimation. Traditionally, the NPP estimation using MODIS or AVHRR data can monitor the vegetation dynamics in a continuous time series, while the coarse spatial resolution of those sensors limit their ability to detect the subtle ecological processes. The subtle ecological processes, which occur at a spatial scale that is lower than the coarse spatial resolution, are more suitable for sensors with high spatial resolutions (e.g., Landsat), but the longer revisit cycle of these sensors and cloud cover hinder efforts to monitor the vegetation change in a timely manner, especially in the period of the growing season. To take both temporal and spatial information into consideration, the spatiotemporal fusion algorithm, such as the Spatial and Temporal Adaptive Reflectance Fusion Model (STARFM) and the Enhanced STARFM (ESTARFM), which can integrate the superiority of multi-source satellites with fine spatial resolutions or frequent temporal coverage and generate dense time series and high spatial resolution data with spatial resolution that is similar to high spatial resolution data, and with temporal resolution that is the same as the high temporal resolution source data, provide a feasible way to solve the "spatiotemporal contradiction" of different remotely sensed datasets. Therefore, this paper attempts to estimate NPP at high spatiotemporal resolution using STARFM and ESTARFM algorithm.

The Pearl River Delta has witnessed the rapid socio-economic development and population growth since the China's reform and opening, accompanied by the massive urban land development. The Statistical Yearbook of Guangdong (2015) showed that the Gross Domestic Product (GDP) of the Pearl River Delta amounted to RMB 5.77 trillion, accounting for 9% of the China's economic aggregates (Guangdong Statistics Bureau, 2015). The World Bank reported that in terms of size and population, the Pearl River Delta has become the largest metropolitan area in the world since 2010, overtaking Tokyo, Japan (http://www.jiemian.com/article/232718.html). The rapid growth of urban areas inevitably caused the deterioration of ecological environment. Therefore, we took the Pearl River Delta as a case to assess the influence of urban sprawl on NPP at a fine resolution. Our goals were tried to settle the following questions: (1) what's the NPP difference at the different spatial resolutions? (2) How did urban sprawl affect the NPP at a fine resolution during 2001–2009? (3) How does the NPP vary under the influence of future urban sprawl at a fine resolution?

2. Data and methods

2.1. Study area

The Pearl River Delta (21.5°N–24°N, 112°E–115.5°E), located in the south-central of the Guangdong Province, is called as "the South Gate" of China (Fig. 1). It covers an area of 41,700 km^2, and consists of the cities of Guangzhou, Foshan, Dongguan, Zhongshan, Shenzhen, Zhuhai, Huizhou, Zhaoqing, and Jiangmen. In this region, the primary climate is the subtropical monsoon climate, characterized by a warm and humid environment, with an average annual temperature of 21–23 °C and an annual rainfall of 1600–2000 mm. The dominant vegetation types are forest and cropland, among which the main forest is evergreen broad-leaved forest and the main crop is rice. The zonal soils are mostly latosolic red and red soil developed by sandstone, shale and granite.

In the study, we selected the core area of the Pearl River Delta, which was one of the areas with the highest levels of urbanization in China, as a representative region, including the cities of Guangzhou, Shenzhen, Foshan, Zhongshan, and Dongguan (Fig. 1).

2.2. Data sources and preprocessing

2.2.1. Datasets for the fusion model

As the input to STARFM and ESTARFM, the Landsat and MODIS images were selected based on the least amount of cloud (cloud cover <10%). The Landsat TM/ETM+ images were downloaded from United States Geological Survey (USGS) (http://glovis.usgs.gov/). To obtain the real surface reflectance, atmospheric correction was conducted on the Landsat images using the Second Simulation of the Satellite Signal in the Solar Spectrum (6S) model. The MODIS product closer to the observation time of Landsat images were selected as the base MODIS images. 16-day composite MODIS NDVI product (MOD13A1) covering the study area were also obtained from the USGS and were reprojected into the same coordinate system as the Landsat images using MODIS

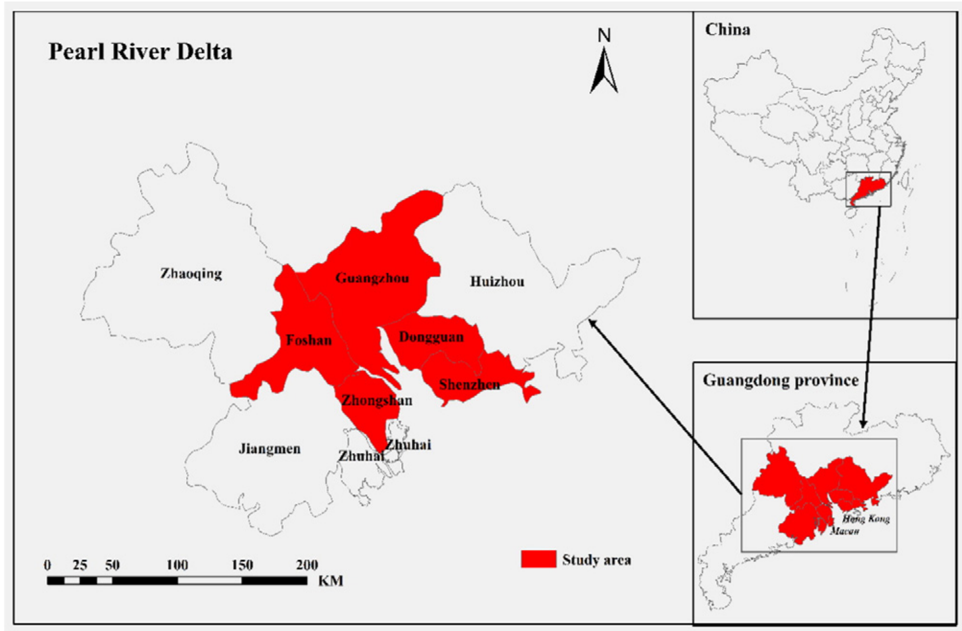

Fig. 1. Location of the Pearl River Delta in China.

Reprojection Tool (MRT), clipped to the same size as the available Landsat images, and further resampled to a 30-m spatial resolution. Additionally, the ESTARFM was used as the main fusion model because it was developed on the basis of STARFM to solve the difficulties in heterogeneous landscapes (Zhu et al., 2010), such as urban areas. The STARFM was utilized when only one pair of Landsat and MODIS images could be used. The way that we used the STARFM and ESTARFM was in agreement with Emelyanova et al. (2013) and Dong et al. (2016) who also applied the two models to their study. Detailed information on data fusion is shown in Tables 1 and 2. As the synthetic NDVI time series still needed to be smoothed to remove the noise (e.g., cloud contamination) before being used for NPP estimation, the Savitzky–Golay (S-G) filtering technique was applied to smooth every pixel's time series profile using TIMESAT software (Jönsson and Eklundh, 2004).

Table 1
Base pair images used in the generation of synthetic NDVI time series in 2001.

Date for data fusion	Input image pairs		Algorithm
	Landsat	MODIS	
2001/01/01			STARFM
2001/01/17			
	2001/01/20	2001/01/17	
2001/02/02			ESTARFM
2001/02/18			
	2001/02/21	2001/02/18	
2001/03/06			ESTARFM
2001/03/22			
2001/04/07			
2001/04/23			
2001/05/09			
	2001/05/12	2001/05/09	
2001/05/25			ESTARFM
2001/06/10			
2001/06/26			
2001/07/12			
2001/07/28			
2001/08/13			
2001/08/29			
2001/09/14			
	2001/09/17	2001/09/14	
2001/09/30			ESTARFM
2001/10/16			
2001/11/01			
2001/11/17			
	2001/11/20	2001/11/17	
2001/12/03			ESTARFM
2001/12/19			
	2001/12/22	2001/12/19	

2.2.2. Datasets for the NPP estimation

2.2.2.1. Mapping the land cover. Landsat TM/ETM + images acquired in 2001 and 2009 were interpreted to describe the land cover using the maximum likelihood classification based on Food and Agriculture Organization-Land Cover Classification System (FAO LCCS), which is a

Table 2
Base pair images used in the generation of synthetic NDVI time series in 2009.

Date for data fusion	Input image pairs		Algorithm
	Landsat	MODIS	
	2009/01/02	2009/01/01	
2009/01/01			ESTARFM
2009/01/17			
2009/02/02			
	2009/02/03	2009/02/02	
2009/02/18			ESTARFM
2009/03/06			
2009/03/22			
2009/04/07			
2009/04/23			
2009/05/09			
2009/05/25			
2009/06/10			
2009/06/26			
2009/07/12			
	2009/07/13	2009/07/12	
2009/07/28			ESTARFM
2009/08/13			
2009/08/29			
2009/09/14			
2009/09/30			
2009/10/16			
2009/11/01			
	2009/11/02	2009/11/01	
2009/11/17			STARFM
2009/12/03			
2009/12/19			

comprehensive, standardized, priori classification system that enables comparison and correlation of land cover classes identified anywhere in the world, at any mapping scale or level of detail (http://dwms.fao.org/~draft/metho_lccs_en.asp). To meet the requirements of the CASA model, the land cover types were reclassified into several new classes: forest (EBF, evergreen broad-leaved forest; DBF, deciduous broad-leaved forest; ENF, evergreen needle-leaved forest; DNF, deciduous needle-leaved forest; MF, mixed forest; Shrub), urban land, cropland, grassland, unused land and water area. The classification results were verified and modified based on field survey data. The overall classification accuracy is 86.75% for the 2001 map and 83.90% for the 2009 map. In addition, as a comparison task, the MODIS land cover type product (MCD12Q1) that cover the years 2001 and 2009 were downloaded from the Earth Observing System (EOS) Data Gateway at the Land Processes Distributed Active Archive Center (LP DAAC) (https://lpdaac.usgs.gov/) to facilitate the NPP estimation at 500-m spatial resolution.

2.2.2.2. Meteorological and soil properties data. The required Meteorological data (e.g., monthly average temperature, monthly total rainfall and monthly total solar radiation) in 2001 and 2009 were attained from the Chinese Meteorological Administration (CMA) (http://data.cma.cn/). These data were collected by 65 meteorological stations and 22 solar radiation observation stations of Guangdong and nearby provinces. The soil properties data (e.g., soil moisture, soil depth, and the ratio of sand and clay) were obtained from the Harmonized World Soil Database (HWSD) (http://westdc.westgis.ac.cn/), which was also developed by FAO of the United Nations (UN). The climate and soil datasets, as the input into the CASA model, were reprojected to the same coordinate system, interpolated to the same spatial resolution and clipped to the same size as the NDVI data using ArcGIS10.2.

2.2.2.3. Measured NPP data. The measured NPP data are used to validate the NPP estimation. This data were mainly derived from two sources: (1) a continuous national forest-inventory data, which were gathered and sorted by China's Ministry of Forestry, and were widely used in previous studies (Luo, 1996; Ni, 2003; Feng et al., 2007; Pei et al., 2013); (2) a continuous provincial forest-inventory data, which were collected by Forestry Surveying and Designing Institute of Guangdong Province, and were also widely used by researchers (Ye and Yu, 2010; Wang et al., 2016). The reasons for the selection of these data are as follows: (a) a continuous measurements were implemented in the period of the growing season for a year or longer; (b) both the aboveground and underground biomass were fully measured. In the records, NPP is presented in units of dry matter (DM), which usually needs to be converted to carbon content (g C/m^2) by using a conversion coefficient of 0.5 for woody biomass (Myneni et al., 2001).

2.2.3. Datasets for the FLUS model

As the input to FLUS model, the vector data of railway, freeway, national highway, provincial highway, ordinary highway, river, airport, city and town were obtained by vectorizing the administrative map of the study area. Digital Elevation Model (DEM) with 30-m spatial resolution was originated from the USGS. The socio-economic data (e.g., GDP, population and economic growth) were derived from the Statistical Yearbook of Guangdong (Guangdong Statistics Bureau, 2001, 2009).

2.3. Methods

2.3.1. CASA model

In this paper, the NPP was estimated using CASA model, which was developed based on the concept of light use efficiency (LUE) (Monteith, 1972; Potter et al., 1993). The CASA model is the product of photosynthetic available radiation absorbed by green vegetation (*APAR*) (MJ·m^{-2}) and the actual LUE (ε) (g C·MJ^{-1}):

$$\mathrm{NPP}(x,t) = APAR(x,t) \times \varepsilon(x,t) \tag{1}$$

where NPP(x,t) (g C/m^2) represents the net primary productivity of pixel x at time t; *APAR* can be described as follows:

$$APAR(x,t) = SOL(x,t) \times FPAR(x,t) \times 0.5 \tag{2}$$

where *SOL* is the total amount of solar radiation (MJ·m^{-2}); *FPAR* is the fraction of photosynthetic active radiation absorbed by vegetation; 0.5 represents half of the incoming solar radiation is in the photosynthetic active radiation (wavelength range of 0.38–0.71 μm).

With regard to *FPAR*, there is a linear function between *FPAR* and *NDVI*:

$$FPAR(x,t) = \frac{(NDVI(x,t) - NDVI_{min})}{(NDVI_{max} - NDVI_{min})} \times (FPAR_{max} - FPAR_{min}) + FPAR_{min} \tag{3}$$

where $NDVI_{max}$ and $NDVI_{min}$ correspond to the maximum and minimum values of *NDVI*. $FPAR_{max}$ and $FPAR_{min}$ are set to the fixed values of 0.001 and 0.95, respectively.

Meanwhile, there is also a linear function between *FPAR* and *SR*:

$$FPAR(x,t) = \frac{(SR(x,t) - SR_{min})}{(SR_{max} - SR_{min})} \times (FPAR_{max} - FPAR_{min}) + FPAR_{min} \tag{4}$$

where SR_{max} is the value of *SR* when all downwelling solar radiation is intercepted, and SR_{min} is the value of *SR* for unvegetated areas. $SR(x,t)$ is shown as a linear function of the *NDVI*:

$$SR(x,t) = \frac{1 + NDVI(x,t)}{1 - NDVI(x,t)} \tag{5}$$

Next, the weighted or direct average of $FPAR-NDVI$ and $FPAR-SR$ can be used as the final result of *FPAR*:

$$FPAR(x,t) = \alpha FPAR_{NDVI} + (1-\alpha) FPAR_{SR} \tag{6}$$

Furthermore, ε is calculated as follows:

$$\varepsilon(x,t) = T_{\varepsilon 1}(x,t) \times T_{\varepsilon 2}(x,t) \times W_{\varepsilon}(x,t) \times \varepsilon_{max} \tag{7}$$

where $T_{\varepsilon 1}(x,t)$ (°C) denotes the limitation of extreme low and high temperature on LUE; $T_{\varepsilon 2}(x,t)$ (°C) denotes the decreases trend of LUE when the environment temperature deviates from the optimum temperature $T_{opt}(x)$ (°C) to extreme low and high temperature.

$$T_{\varepsilon 1}(x,t) = 0.8 + 0.02 \times T_{opt}(x) - 0.0005 \times \left[T_{opt}(x)\right]^2 \tag{8}$$

$$T_{\varepsilon 2}(x,t) = \frac{1.184}{\left\{1 + e^{\left[0.2\left(T_{opt}(x) - 10 - T(x,t)\right)\right]}\right\} \times \left\{1 + e^{\left[0.3\left(-T_{opt}(x) - 10 + T_{(x,t)}\right)\right]}\right\}} \tag{9}$$

The moisture stress coefficient $W_{\varepsilon}(x,t)$ denotes the limitation of moisture on LUE, and is determined by a function of Estimated Evapotranspiration (*EET*, mm) and Potential Evapotranspiration (*PET*, mm):

$$W_{\varepsilon(x,t)} = 0.5 + \frac{0.5 \times EET(x,t)}{PET(x,t)} \tag{10}$$

where $EET(x,t)$ (mm) (Estimated Evapotranspiration) is derived from a one-layer bucket soil moisture model (Potter et al., 1993), which is

Table 3
The ε_{max} of typical vegetation types in the Pearl River Delta (Jiang et al., 2015).

Vegetation types	ε_{max} (g C·MJ^{-1})	Vegetation types	ε_{max} (g C·MJ^{-1})
Cropland	0.455	Urban land	0.482
EBF	0.808	Grassland	0.482
DBF	0.585	Shrub	0.389
ENF	0.378	Others	0.482
DNF	0.434		
MF	0.461		

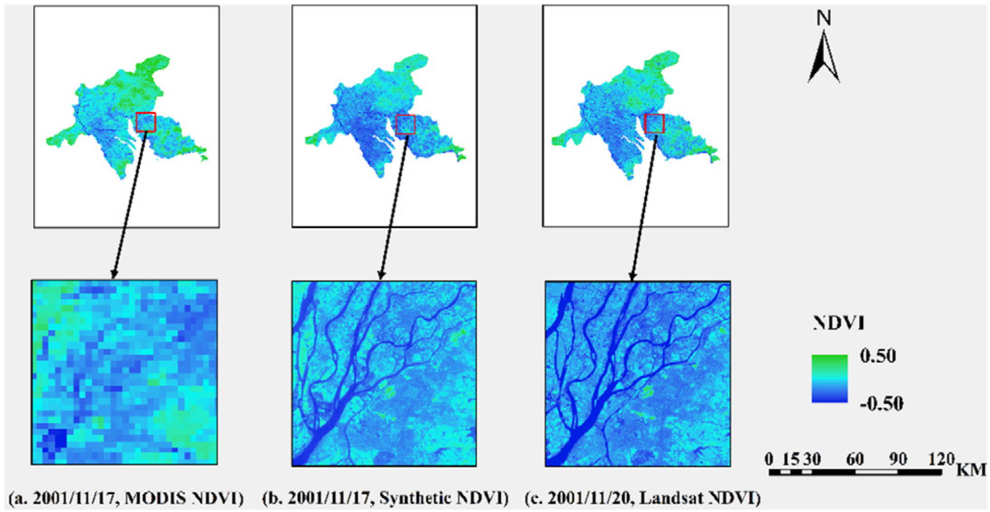

Fig. 2. Comparison of synthetic NDVI derived from ESTARFM and observed NDVI.

estimated using monthly temperature and rainfall combined with soil properties data, and $PET(x,t)$ (mm) (Potential Evapotranspiration) is calculated by the method of Thornthwaite (1948).

The ε_{max} (g C·MJ^{-1}) is the maximum LUE of vegetation under the optimal environment conditions (Bradford et al., 2005). We refer to Jiang et al.'s (2015) results about the ε_{max}values of typical vegetation types in the Pearl River Delta (Table 3).

2.3.2. Spatiotemporal fusion of remotely sensed data

The STARFM was developed to produce fine-resolution (Landsat-like) images for desired prediction dates (t_p) by computing the spatially weighted difference between the fine-resolution (Landsat) and coarse-resolution (MODIS) images on the base date (t_m), and the fine-resolution (Landsat) t_m-scene and one or more coarse-resolution (MODIS) images of the prediction dates (t_p) (Gao et al., 2006). Subsequently, Zhu et al. (2010) developed the ESTARFM by employing two pairs of contemporaneous fine-resolution (Landsat) and coarse-resolution images (MODIS) acquired on the base date t_m, t_n. Compared with STARFM, the major difference of ESTARFM is the introduction of a conversion coefficient of similar pixels in the contemporaneous fine-resolution (Landsat) and coarse-resolution (MODIS) images (Zhu et al., 2010). Recently, it has been shown that the accuracy of synthetic NDVI images, generated using the Landsat and MODIS NDVI images directly as inputs for fusion model ("index then blend"), is generally higher than the fusion model-generated NIR (near infrared) and red band of Landsat-like images ("blend then index") (Jarihani et al., 2014; Olexa and Lawrence, 2014; Tian et al., 2013), so we chose the "index then blend" approach to generate the synthetic NDVI.

To evaluate the accuracy of synthetic NDVI achieved by the ESTARFM and STARFM in our study, available Landsat and MODIS images were applied. With regard to ESTARFM, two pairs of Landsat data (2001/09/17 and 2001/12/22) and MODIS data (2001/09/14 and 2001/12/19) acquired on the base date and a set of MODIS data (2001/11/17) acquired on the prediction date were fused using the ESTARFM algorithm to generate the predicted Landsat-NDVI on the prediction date (2001/11/17). Then, the observed Landsat-NDVI (2001/11/20) was used to assess the accuracy of the predicted Landsat-NDVI. Fig. 2a–c represent the MODIS NDVI (observed MODIS-NDVI), the synthetic NDVI (predicted Landsat-NDVI), and the Landsat NDVI (observed Landsat-NDVI), respectively. Visual observation shows that the synthetic NDVI, with more detailed spatial information, has a higher spatial resolution than MODIS NDVI and is very similar to TM NDVI. Fig. 4a shows that the scatter plot of the synthetic and Landsat NDVI for ESTARFM fits well with the y = x lines, with $R^2 = 0.785$ and RMSE = 0.068. Likewise, with regard to STARFM, one pair of Landsat data (2001/02/21) and MODIS data (2001/02/18) was used as the base images, and a MODIS image (2001/01/17) as the image for prediction. Then, the synthetic NDVI was validated using the observed Landsat NDVI (2001/01/20).

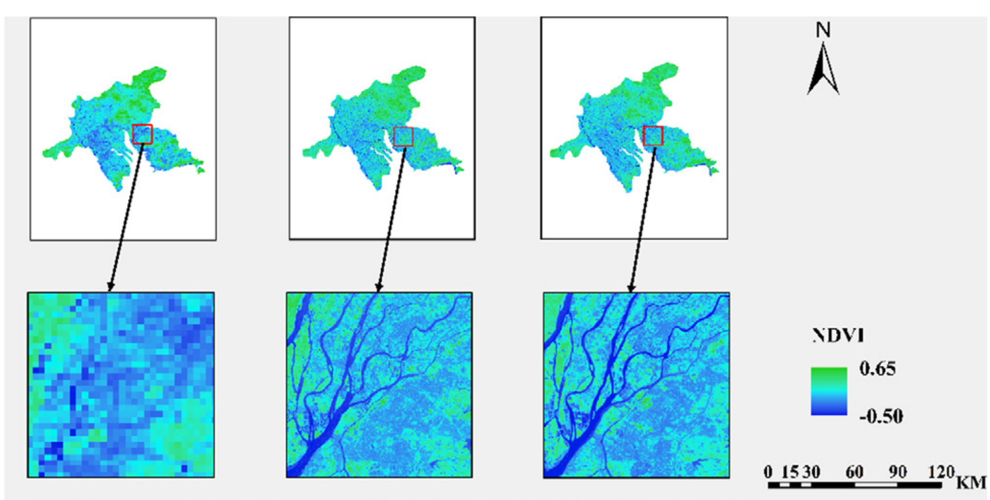

Fig. 3. Comparison of synthetic NDVI derived from STARFM and observed NDVI.

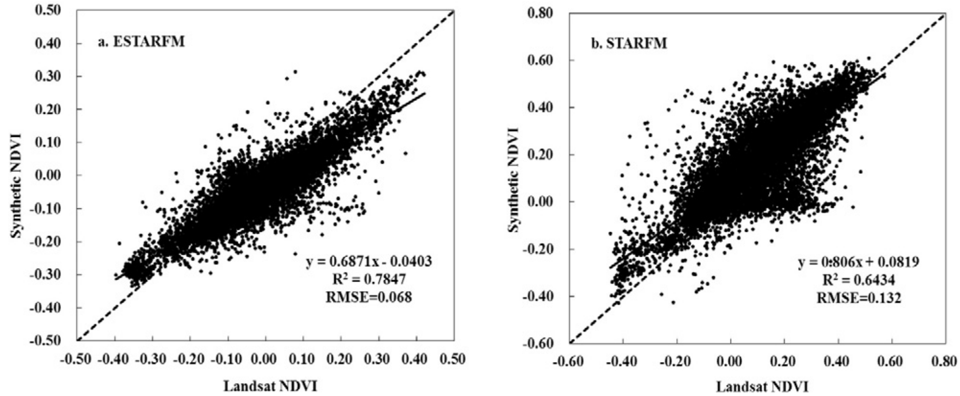

Fig. 4. Evaluating the accuracy of synthetic NDVI for ESTARFM and STARFM.

We found similar results in the STARFM as the ESTARFM (Figs. 3 and 4b). These results indicate that a high similarity between the predicted and observed Landsat-NDVI, and a high accuracy of the ESTARFM and STARFM algorithm in generating predicted Landsat-NDVI. Note that we refer to the results of the synthetic NDVI with high spatiotemporal resolution used as the input for the CASA model as the "30-m resolution NPP". The results of the MODIS NDVI with coarse spatial resolution but frequent coverage used as the input for the CASA model is defined as the "500-m resolution NPP".

2.3.3. FLUS model

The FLUS model is an integration of a top-down System Dynamics (SD) model and a bottom-up multiple Cellular Automata (CA) model. The SD model is used to project the land use demands by considering both human activities (e.g., GDP, population, railway, highway) and natural factors (e.g., global warming, precipitation variations) on account of the natural factors will have a significant impact on land use dynamics in the long-term. A self-adaptive inertia and competition mechanism is developed within the CA model to handle the complex competitions and interactions among different land use types. Liu et al. (2017) indicated that the FLUS model was able to simulate the land use dynamics in a more realistic manner, and was superior to the Conversion of Land Use and its Effects at Small regional extent (CLUE-S) model and the Artificial Neural Network and Cellular Automata (ANN-CA) model in the Pearl River Delta. The flow chart of the FLUS model is illustrated in Fig. 5. The GeoSOS-FLUS software was also developed to facilitate the LUCC simulations (available for downloading at: http://www.geosimulation.cn/flus.html).

The FLUS model was used to simulate the process of urban sprawl from 2009 to 2050 under Baseline Development (BD)-Scenario, Fast Development (FD)-Scenario, Slow Development (SD)-Scenario and Harmonious Development (HD)-Scenario. The BD-Scenario is assumed that the current trends of economic development, population growth and technological innovation, and the current situation of temperature and precipitation remain continue into the future. The FD-Scenario is designed that the economy and population increase at a high speed, and the technology develop rapidly. Meanwhile, the sharp increase of temperature and precipitation occurs in this scenario. Contrary to the FD-Scenario, the SD-Scenario is constructed under the influence of low-speed socio-economic growth and smaller climate change. The

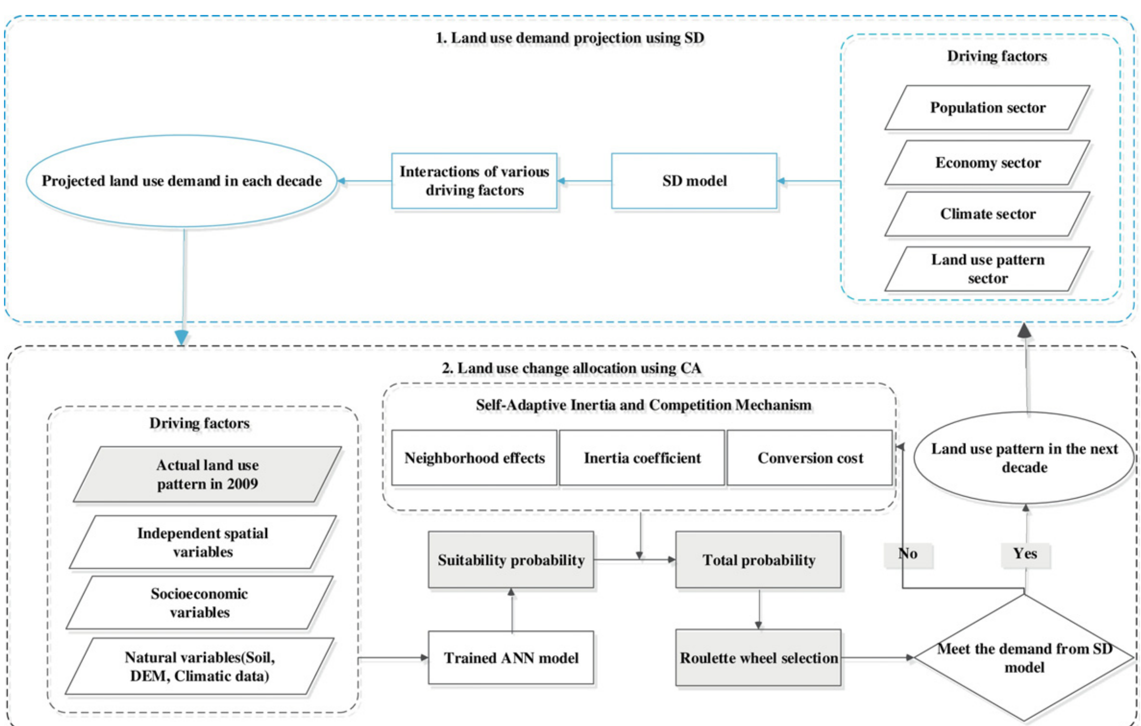

Fig. 5. Flow chart of the FLUS model.

Table 4
Parameter determination of various factors for the four scenarios in the south humid domain of China (Liu et al., 2017).

	Scenarios	BD-Scenario	FD-Scenario	SD-Scenario	HD-Scenario
Factors	Population growth (%/a)	0.62	0.76	0.47	0.47
	Economic growth (%/a)	7.00	7.97	5.20	6.91
	Technological innovation (%/a)	10	15	5	20
	Rainfall change (mm/a)	0.4770	0.6970	0.0188	0.6596
	Temperature change (°C/a)	0.0452	0.0817	0.0044	0.0683

last one, the HD-Scenario is developed based on the moderate growth of the economy and population, and the high-speed of technological innovation. Moreover, the climate will change moderately. We refer to Liu et al.'s (2017) detailed description of the parameter determination of various socio-economic and natural factors for the four scenarios in the south humid domain of China (Table 4).

2.4. Study process

This study includes the following three components: (1) Variations of urban areas; (2) comparison of NPP at different spatial resolutions; and (3) impacts of urban sprawl on NPP at a fine resolution. Furthermore, this component is also implemented in three steps as follows: 1) Seasonal NPP variations due to urban sprawl; 2) NPP loss induced by urban sprawl during 2001–2009; and 3) NPP loss induced by urban sprawl from 2009 to 2050. The flow chart of this study is shown in Fig. 6.

3. Results and discussion

3.1. Variations of urban land

Fig. 7a shows the variations of land cover types. The areas of water, forest, cropland, grassland, and unused land showed decreasing trends from 2001 to 2009, with reduction of 585.95 km^2, 566.82 km^2, 1392.45 km^2, 94.21 km^2, 6.7 km^2, respectively. Of all land cover types, cropland had the largest reduction in area. On the contrary, the area of urban land dramatically expanded from 3447.72 km^2 in 2001 to 6093.99 km^2 in 2009 with an annual increase in area of 294.03 km^2 and an annual increase rate of 8.53%, suggesting a rapid urban sprawl in the Pearl River Delta.

Rapid urban sprawl came at the expense of massive occupation of productive land. Fig. 7b shows the percentages of urban land converted from non-urban land. Obviously, cropland was the primary contributor to urban sprawl, accounting for 56.87% of the urban sprawl. The encroachment of urban areas into cropland could greatly destroy the crop productivity, and even lead to a food crisis (Liu et al., 2005). Forest accounted for 23.81% of the urban sprawl, with evergreen broad-leaf forest representing the largest proportion (15.02%), indicating a serious deforestation due to urbanization. Water area accounted for 16.08% of the urban sprawl. Ye and Dong (2010) reported that water area had relatively higher coefficient of sensitivity (CS) of ecological value and played an important role in ecosystem services in the Pearl River Delta. Thus, the protection of water area should gain more attention. What's more, grassland and unused land accounted for a lower proportion because of their smaller areas. These results showed that cropland was the largest contributor to the urban sprawl, followed by forest and water area.

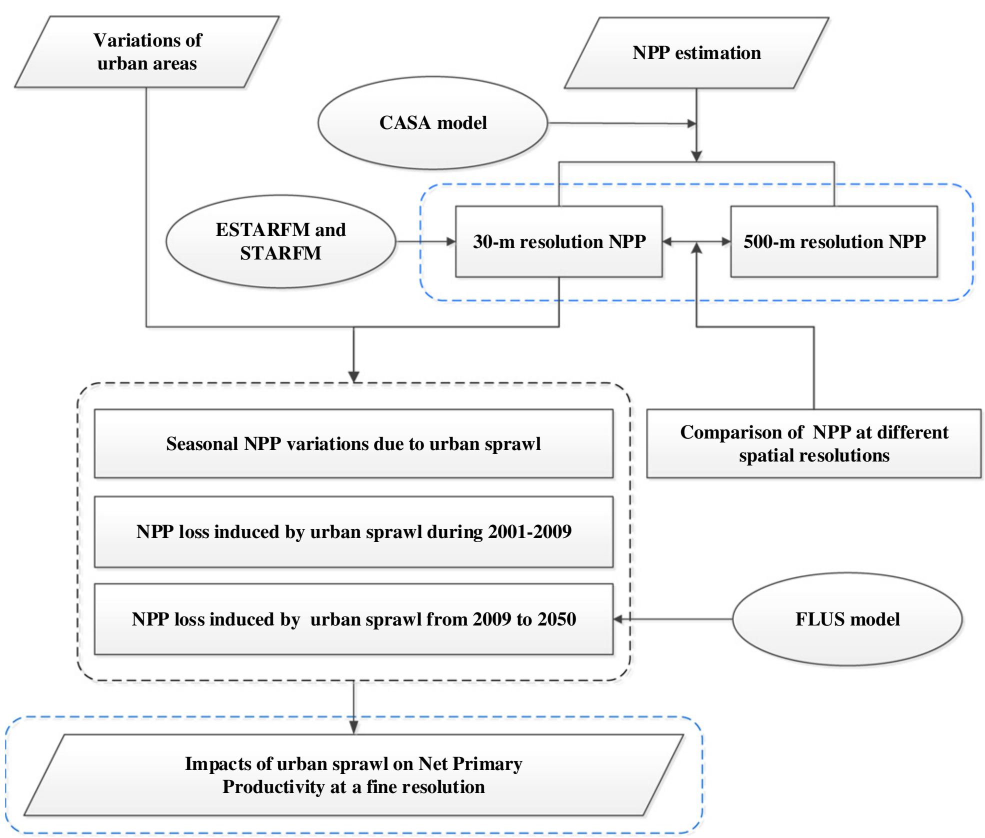

Fig. 6. Flow chart of this study.

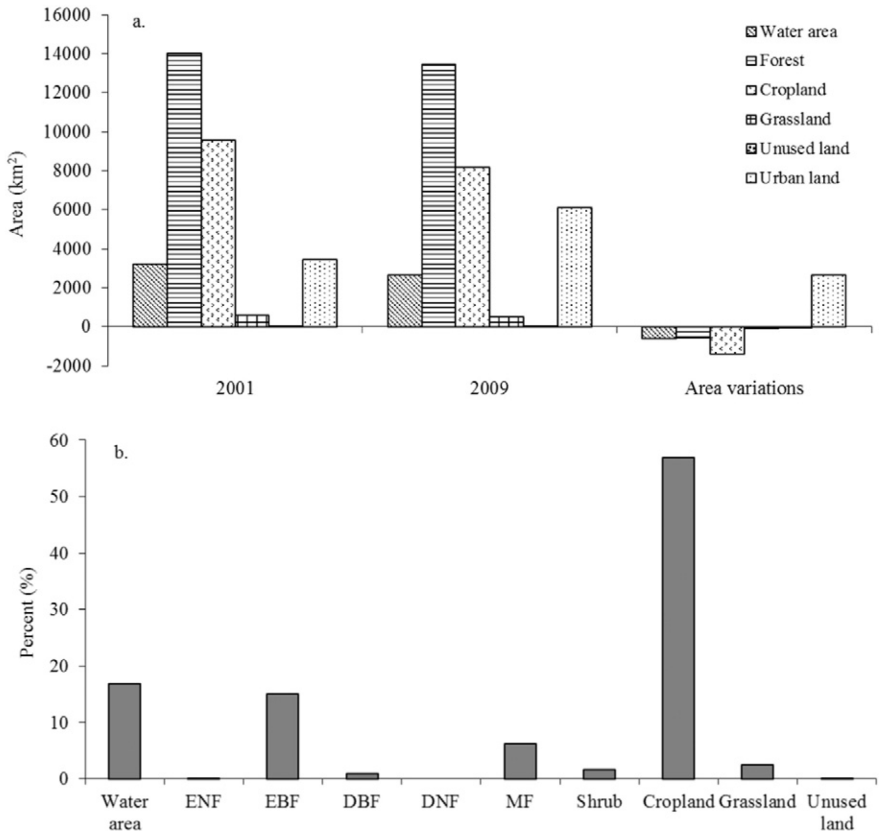

Fig. 7. (a) Area variations in land cover types during 2001–2009; (b) percentages of urban land converted from non-urban land during 2001–2009. refer to Table 3 about the legend description.

3.2. Comparison of NPP at different spatial resolutions

3.2.1. Validation of the NPP estimation

To validate our NPP estimation, we first made a comparative analysis of NPP at different spatial resolutions calculated by us and other researchers in the study area. As shown in Table 5, the mean values of 30-m and 500-m resolution NPP were 564.52 g C/m^2 and 586.63 g C/m^2, respectively, closing to the results of Jiang et al. (2015) and Pei et al. (2013), and MOD17A3 product (https://ladsweb.nascom.nasa.gov/). Furthermore, a comparison between estimated and measured NPP was also conducted. As shown in Fig. 8a and b, there is good agreement between 30-m resolution NPP and measured data, with a strong linear correlation (R^2 = 0.871 and RMSE = 79.36 g C/m^2; Fig. 8a). 500-m resolution NPP also showed good agreement with the measured data, with R^2 of 0.826 and RMSE of 91.38 g C/m^2 (Fig. 8b). The result for 30-m resolution NPP showed an improvement of 0.045 in R^2 and a reduction of 12.02 g C/m^2 in RMSE compared with 500-m resolution NPP, indicating that the accuracy of 30-m resolution NPP is better than 500-m resolution NPP and the spatiotemporal fusion algorithm can improve the accuracy of NPP estimation.

3.2.2. Detectability of the 30-m resolution NPP

To explore the detectability of the 30-m resolution NPP, we continued to make a comparative analysis of the 30-m and 500-m resolution NPP. Fig. 9a and b show the spatial distribution of the 30-m and 500-m resolution NPP. The spatial variations of NPP exhibit an overall decrease from the North, which is mostly covered by vegetation, to the South, which is mostly covered by urban areas. The 30-m resolution NPP displays more detailed spatial information at a fine spatial scale. For example, the river, forest and building areas all show preferable textural features. Whereas, in the 500-m resolution NPP, it is difficult to distinguish the spatial heterogeneity of the surface at a fine spatial scale.

Fig. 10 shows the NPP difference between urban and non-urban areas at the 30-m and 500-m resolution. The mean NPP of urban and non-urban areas at the 30-m resolution were 220.83 g C/m^2 and 712.50 g C/m^2, respectively. The mean NPP of urban and non-urban areas at 500-m resolution were 314.45 g C/m^2 and 696.93 g C/m^2, respectively. The difference between the two regions was 491.67 g C/m^2 for the 30-m resolution NPP and 382.48 g C/m^2 for the 500-m resolution NPP. This result indicated that the NPP difference between the two regions enlarged with the improvement of the spatial resolution. This was mainly because the 500-m resolution NPP, characterized by the abundance of urban and non-urban land mixed pixels, had a relatively weakened ability to detect NPP difference at a fine spatial scale. Conversely, the 30-m resolution NPP could detect the information on boundaries between the two regions accurately, and further improve the ability to detect the NPP difference. Moreover, the large NPP difference between the two regions also indicated that the mean NPP was much lower in urban than in non-urban areas. Thus, the conversion of non-urban to urban areas would lead to a large loss in NPP, a finding

Table 5
Comparison of NPP at different spatial resolutions estimated by us and other researchers (g C/m^2).

Model	Spatial resolution	NPP values	Data sources
CASA	250 m × 250 m	553.80	Jiang et al. (2015)
CASA	1000 m × 1000 m	550.9 ± 148.2	Pei et al. (2013)
BIOME-BGC	1000 m × 1000 m	526.70	MOD17A3
CASA	500 m × 500 m	586.63	This study
CASA	30 m × 30 m	564.52	This study

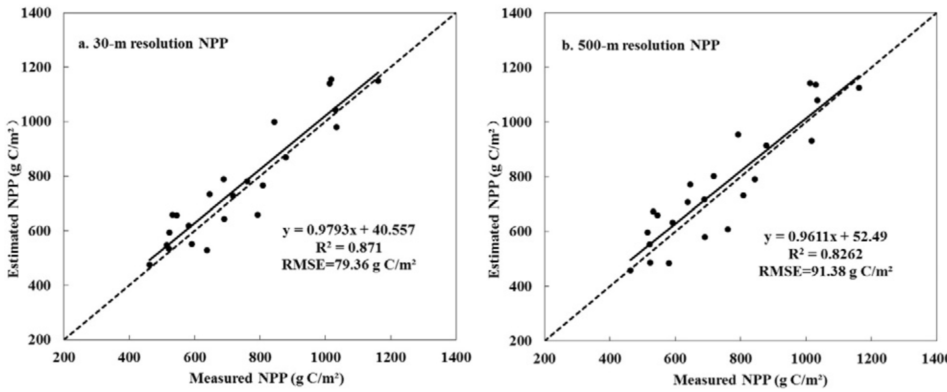

Fig. 8. Comparison of NPP at different spatial resolutions and measured data (g C/m^2).

that prompted us to explore the influence of urban sprawl on NPP further.

To further test the detectability of the 30-m resolution NPP, we compared the NPP at the 30-m (resampled to 500-m) and 500-m resolution according to the different percentage of urban land in a grid cell with a size of 500 m × 500 m. As shown in Fig. 11, the time-sequence curve of 30-m resolution NPP showed a similar monthly dynamic characteristic as 500-m resolution NPP under the different percentage of urban land. More importantly, the monthly NPP difference between the 30-m and 500-m resolution decreased with the increasing percentage of urban land. On the one hand, when the percentage of urban land was higher than 60% (Fig. 10d and e), the time-sequence curve of 30-m resolution NPP was closer to the 500-m resolution NPP because of an aggregated and compact distribution of urban land lacking vegetation cover. On the other hand, when the percentage of urban land was <40%, the 500-m resolution NPP was obviously greater than the 30-m resolution NPP (Fig. 10a and b). The NPP at the coarse resolution being overestimated was also confirmed by previous studies (Singh, 2011; Hwang et al., 2008). This was mainly because in the areas with the lower percentage of urban land, many smaller and highly fragmented urban lands at the sub-MODIS pixel scale, which embedded in the trees and scattered in the mountains, were difficult to be detected at the 500-m resolution and thus easy to be mistaken for non-urban land with higher NPP. Alternatively, in the 30-m resolution NPP, the urban land with lower NPP could be detected accurately. Therefore, the detectability of the 30-m resolution NPP was superior to the 500-m resolution NPP. Additionally, these results also proved that the 30-m resolution NPP not only obtained the sequential temporal information from MODIS data, but also acquired the detailed spatial information from Landsat data successfully.

3.3. Impacts of urban sprawl on NPP

3.3.1. Seasonal NPP variations due to urban sprawl

To analyze the seasonal variations of 30-m resolution NPP influenced by urban sprawl, the monthly and seasonal NPP for urban and non-urban areas and the monthly NPP difference between the two regions were calculated. As shown in Fig. 12a, the mean NPP of urban

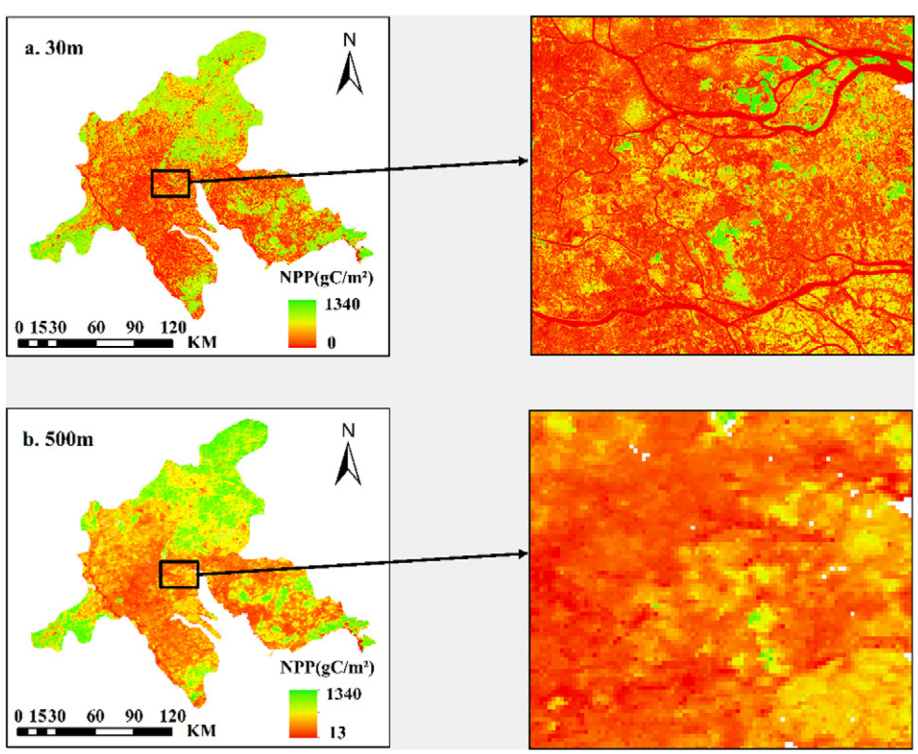

Fig. 9. NPP distribution at different spatial resolutions in 2009.

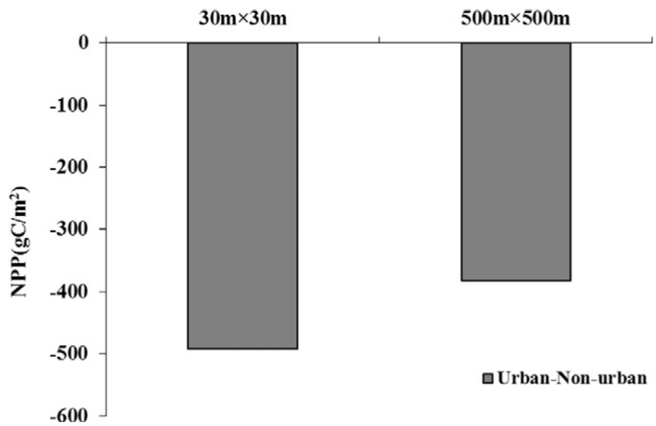

Fig. 10. NPP difference between urban and non-urban areas at different spatial resolutions.

areas showed a similar monthly dynamic characteristic as the non-urban areas. More specifically, it showed a clear increasing trend from March to July mainly due to the increases of temperature and rainfall in this period of time, and then exhibited an obvious decreasing trend from August to December because of the relatively lower temperature and rainfall. As shown in Fig. 12b, the mean NPP of urban areas in spring (March to May), summer (June to August), autumn (September to November) and winter (December to February) were 43.11 g C/m^2, 95.71 g C/m^2, 63.13 g C/m^2, 19.00 g C/m^2, and of the corresponding non-urban areas were 143.15 g C/m^2, 319.46 g C/m^2, 207.10 g C/m^2, 71.40 g C/m^2, respectively. We could see that the mean NPP of urban areas also showed a similar seasonal dynamic characteristic as the non-urban areas. Namely, the NPP value peaked in summer, and reached its minimum in winter.

The positive or negative influences of urban sprawl on NPP mainly depend on the local environment (Pouyat et al., 2007). Most of this region belong to the subtropical monsoon climate associated with favorable temperature and abundant rainfall. There was a symmetric distribution in the monthly NPP difference between urban and non-urban areas throughout a year, where the urban areas had a significantly lower NPP than the non-urban areas every month, and showed a maximum loss in NPP (approximately −80.05 g C/m^2) in July (Fig. 12c). These results were in agreement with Pei et al. (2013) who indicated that urbanization had an adverse impact on NPP in warm and humid regions of China, especially during the peak growing season. Namely, the resource augmentations supported by human (e.g., reasonable irrigation and fertilization for vegetation, introduction of foreign species with high productivity) and the effects of the Urban Heat Island (UHI) and Urban Rain Island (URI) in urban areas may not have significant effects on higher NPP, in comparison to the superior natural conditions

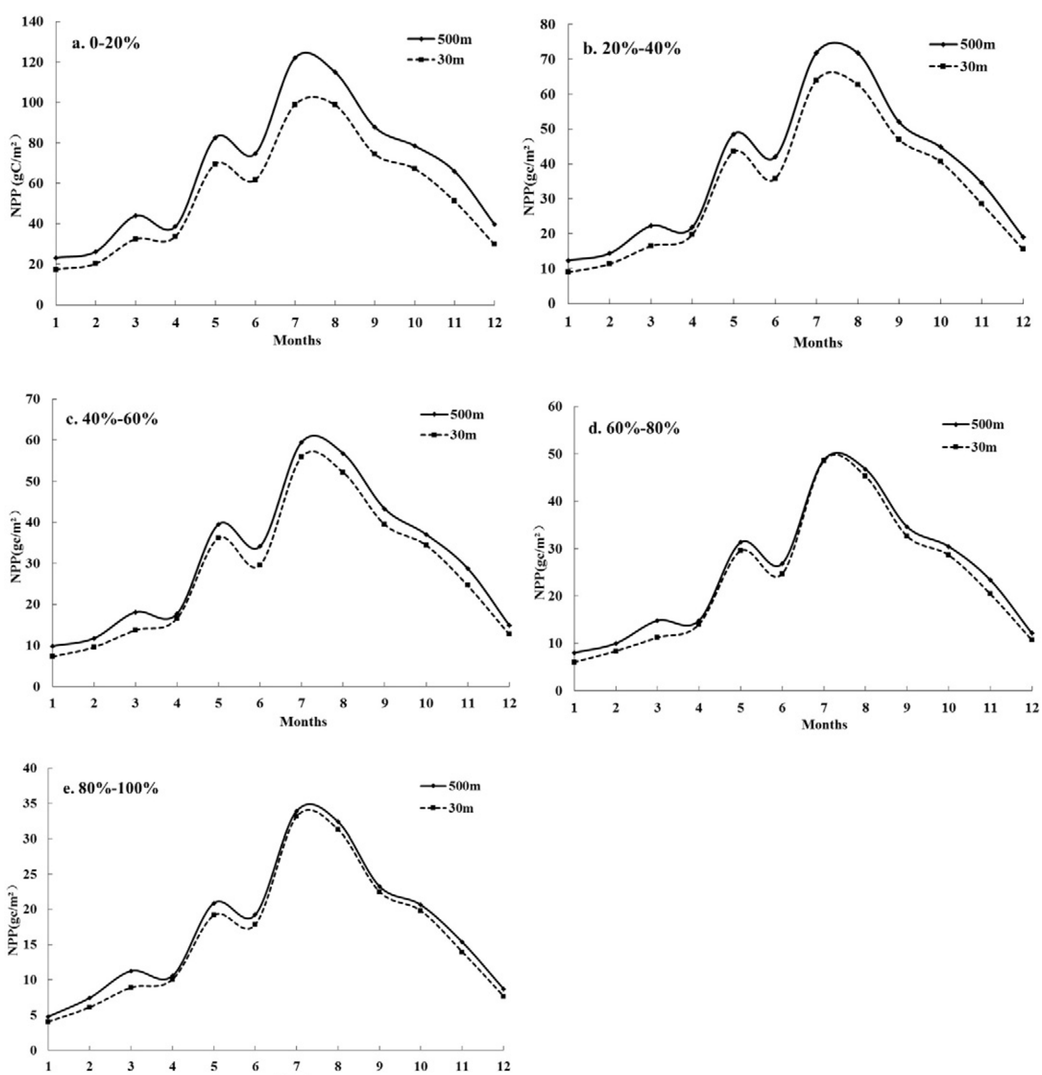

Fig. 11. NPP difference between the 30-m and 500-m resolution under the different percentage of urban land.

occurring in the surrounding non-urban areas. Therefore, urban sprawl may lead to the net loss in 30-m resolution NPP even under favorable climatic conditions.

3.3.2. NPP loss induced by urban sprawl during 2001–2009

The spatiotemporal variations of NPP at different spatial resolutions are shown in Fig. 13a and b. A dense point pattern is more evident at the 30-m resolution due to the fact that the variations of NPP are different between a small piece of urban land at the sub-MODIS pixel scale and its neighbor (i.e., non-urban land), while a faint blocky pattern occurs at the 500-m resolution. Furthermore, the area of NPP reduction at the 30-m resolution was greater than that at the 500-m resolution, particularly in the areas with high vegetation cover (e.g., the north of this region). This was also because many smaller and highly fragmented urban lands change over time could be detected more accurately in the 30-m resolution than in the 500-m resolution NPP.

The NPP loss was calculated by overlaying the difference layer of urban land between 2001 and 2009 with Fig. 13a and b. As shown in Table 6, the total loss of 30-m and 500-m resolution NPP induced by urban sprawl were 349.95 Gg C (1 Gg $= 10^9$ g) and 148.05 Gg C, respectively, indicating that the total loss from the 30-m resolution NPP was significantly higher than the 500-m resolution NPP. According to the equation of photosynthesis and respiration, an increase of 1 g C in vegetation can absorb 1.63 g CO_2 and release 1.2 g O_2 (Yu et al., 2009). The total loss of 349.95 Gg C in the 30-m resolution NPP is equivalent to a reduction in absorption of 570.5 Gg CO_2 and release of 420 Gg O_2 from vegetation. Moreover, the loss of 349.95 Gg C is also equivalent to the heat released by 2.34×10^6 t of standard coal, because the heat contained in 1 g C of vegetation equals that contained in 0.00067 g of standard coal (Yu et al., 2009). Thus, there is a considerable reduction in carbon sink due to urban sprawl.

More specifically, the loss in 30-m resolution NPP induced by the conversion of forest to urban land was 221.54 Gg C, accounting for 63.31% of total NPP loss, which possibly resulting from the higher NPP of forest (approximately 888.01 g C/m^2) and the larger area of forest transformed to urban land. Forest can provide diverse ecosystem services, such as the timber supplying, water and soil conservation, carbon fixation and oxygen release, atmosphere purification (Duncker et al., 2012). Therefore, the forest NPP loss could reduce the multiple ecosystem service functions. The NPP loss because of cropland being transferred to urban land was 133.17 Gg C, accounting for 38.05% of total NPP loss, which could reduce the food supply from the cropland ecosystem. The Pearl River Delta had a prominent contradiction between food supply and demand in China. According to the Statistical Yearbook of Shenzhen, over 95% of food needed to be imported in the city of Shenzhen (Shenzhen Statistics Bureau, 2015). Hence, the sharp reduction of cropland NPP would further threaten the food security of this region. The grassland NPP loss was only 6.64 Gg C because the area of grassland encroached by urban land was small. Nevertheless, the conversion of water area and unused land to urban land led to NPP gains of 11.28 Gg C and 0.12 Gg C, respectively. The NPP of urban land (approximately 220.83 g C/m^2) was relatively higher than the NPP of areas with less vegetation coverage such as water area (approximately 149.19 g C/m^2) and unused land (approximately 204.10 g C/m^2) due to the resource augmentations supported by human and the effects of the UHI and URI (Pei et al., 2013). Thus, the conversion of water area and unused land to urban land led to an increase in NPP. From the above, we also could see that the loss of NPP from the forest and cropland was the main contributor to the total NPP reduction as well as the main reason for the decline in ecosystem service functions.

3.3.3. NPP loss induced by urban sprawl from 2009 to 2050

To assure the ecological services function of this region, we should fully consider the NPP loss induced by future urban sprawl. For this study, we assume that the NPP variations is only affected by urban sprawl in the future without consideration of other factors, such as climate changes, CO_2 fertilization and nitrogen deposition, that is, the average NPP values for different land cover types is constant, so the total

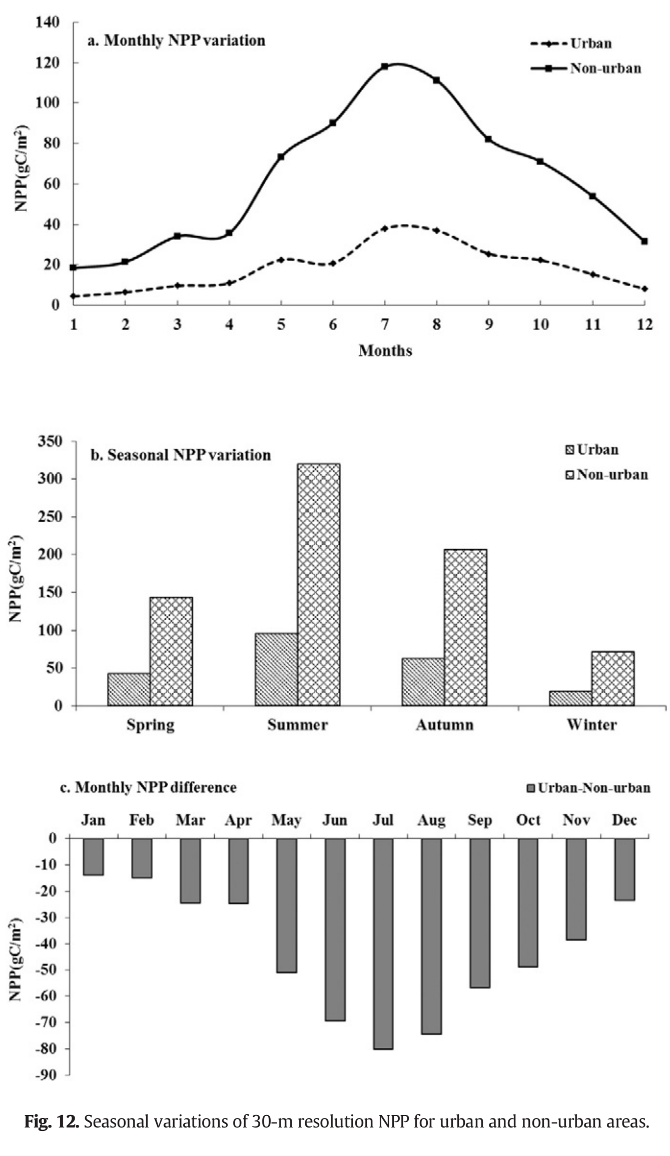

Fig. 12. Seasonal variations of 30-m resolution NPP for urban and non-urban areas.

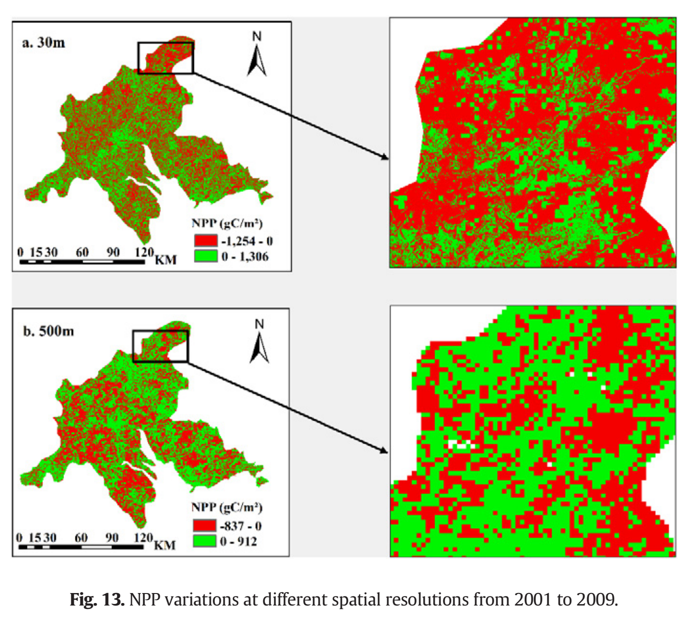

Fig. 13. NPP variations at different spatial resolutions from 2001 to 2009.

Table 6
NPP loss induced by urban sprawl at different spatial resolutions during 2001–2009 (Unit: Gg C). UL, Urban land. The symbol "+" represents an NPP increase, and "−" represents an NPP loss.

Spatial resolutions	Water area −UL	Forest −UL	Cropland −UL	Grassland −UL	Unused land −UL	Total loss of NPP
500 m × 500 m	−16.11 (10.88%)	−45.84 (30.96%)	−83.10 (56.13%)	−3.22 (2.17%)	+0.21 /	−148.05
30 m × 30 m	+11.28 /	−221.54 (63.31%)	−133.17 (38.05%)	−6.64 (1.90)	+0.12 /	−349.95

NPP loss can be calculated by overlaying the layer of newly increased urban land between 2009 and 2050 with the 30 m-resolution NPP distribution in 2009 (Fig. 9a), and then subtracting the total NPP of newly increased urban land.

As shown in Fig. 14a–d, urban land mainly presents as a fringe and infilling growth, and becomes more aggregated and compact under all scenarios. The total area of the urban sprawl under the BD-Scenario, FD-Scenario, SD-Scenario, HD-Scenario are estimated to be about 5781.79 km^2, 7255.69 km^2, 3089.67 km^2, 4309.77 km^2, and the corresponding total NPP loss induced by the urban sprawl are 1161.58 Gg C, 1454.18 Gg C, 486.41 Gg C, 745.25 Gg C, respectively. This results show that under the FD-Scenario and BD-Scenario, the area of the urban sprawl and the corresponding NPP loss are large, this can be explained by a lot of infrastructure will be built to cope with the dramatic socio-economic development and the enormous population growth. These scenarios will develop at the expense of natural resources and ecological environment. Fortunately, the two scenarios may be forbidden in the future by government management, technological progress and the improvement of people's environmental awareness, etc. Under the SD-Scenario, the smallest size of urban sprawl and the corresponding smallest loss in NPP occurs in this region due to the low growth of social-economic and population. This scenario will create an environmental-friendly society. However, it will be impossible to implement because this scenario may lead to a waste of land resources, and the conservative development is also difficult to improve the human well-being. Under the HD-Scenario, a reasonable size of urban sprawl adapts to the moderate socio-economic development and the low population growth. The NPP loss under this scenario is much lower than that under the FD-Scenario and BD-Scenario, and slightly higher than that under the SD-Scenario. Thus, the HD-Scenario, which can strike a balance between the urban sprawl and ecological environment, is a more favorable and sustainable development strategy.

4. Conclusions

In the study area, the area of urban land expanded by 2646.27 km^2 from 2001 to 2009, revealing a rapid urban sprawl of this region. To analyze the influence of urban sprawl on NPP at a fine resolution, the 30-m resolution NPP driven by the spatiotemporal fusion algorithm was estimated. By a comparison of NPP at the 30-m and 500-m resolution, our findings revealed that the spatiotemporal fusion algorithm could improve the accuracy of NPP estimation and the detectability of the 30-m resolution NPP was superior to the 500-m resolution NPP. Urban sprawl led to the NPP loss even under the favorable climatic conditions. The loss in the 30-m resolution NPP induced by urban sprawl was much higher than the 500-m resolution NPP, mainly because of the effective detectability achieved by the 30-m resolution NPP. The NPP loss from forest and cropland accounted for 63.31% and 38.05% of the total NPP reduction and was the primary cause of reducing the ecosystem service functions. Thus, when we delimit the urban growth boundary, the protection of forest and cropland should be given much attention.

To further analyze the NPP variations induced by future urban sprawl at a fine resolution, the process of urban sprawl from 2009 to 2050 under different scenarios were simulated using FLUS model. The FD-Scenario and BD-Scenario may be forbidden because of a serious waste of natural resources and environmental destruction. The SD-

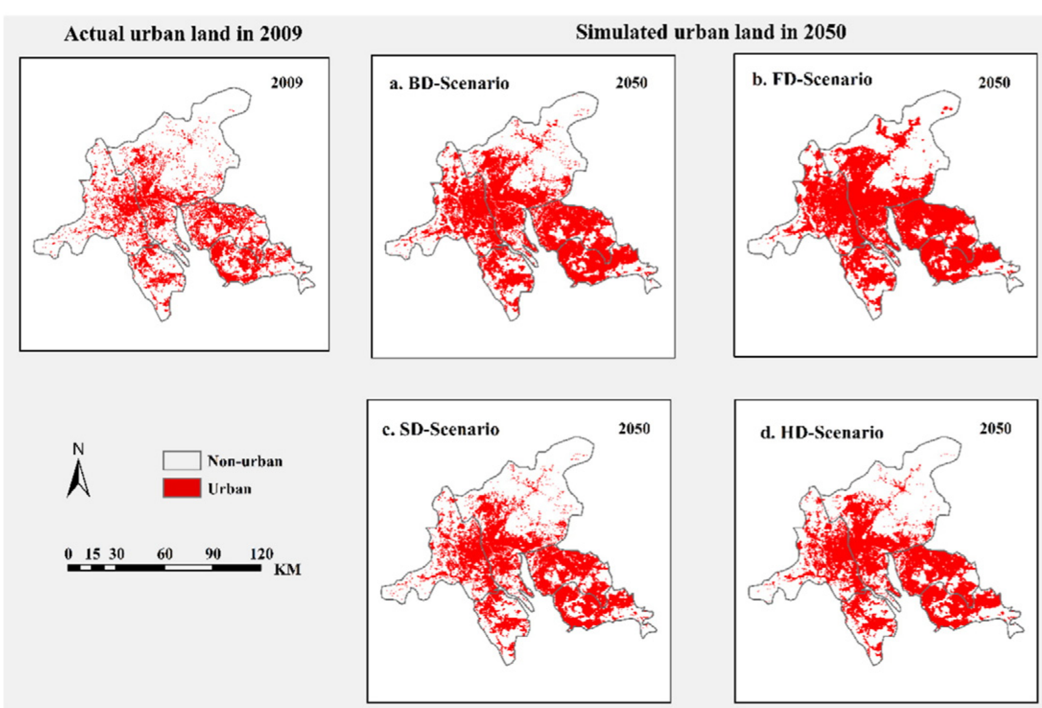

Fig. 14. Simulation of the urban sprawl under different scenarios from 2009 to 2050.

Scenario will be impossible to implement because the conservative development is difficult to improve the human well-being. The HD-Scenario is a more favorable and sustainable development strategy because this scenario can balance the benefits between the urban sprawl and ecological environment.

The primary innovation of this study was that we assessed the influence of urban sprawl on NPP at a fine resolution. Our results would be of great significance for carbon cycle research, and would provide a theoretical foundation for urban planning and management. However, in the actual situation, the NPP was also influenced by many factors of human activities and natural mechanisms other than urban sprawl. Thus, the exploration of the relative contributions of these factors to the NPP variations in detail would be an important topic for future research.

Acknowledgments

This study was supported by the National Key R&D Program of China (Grant No. 2017YFA060442) and the National Natural Science Foundation of China (Grant No. 41671398).

References

Bradford, J.B., Hicke, J.A., Lauenroth, W.K., 2005. The relative importance of light-use efficiency modifications from environmental conditions and cultivation for estimation of large-scale net primary productivity. Remote Sens. Environ. 96 (2), 246–255.
Buyantuyev, A., Wu, J., 2009. Urbanization alters spatiotemporal patterns of ecosystem primary production: a case study of the Phoenix metropolitan region, USA. J. Arid Environ. 73, 512–520.
Buyantuyev, A., Wu, J.G., Gries, C., 2010. Multiscale analysis of the urbanization pattern of the Phoenix metropolitan landscape of USA: time, space and thematic resolution. Landsc. Urban Plan. 94, 206–217.
Canadell, J., Mooney, H.A., 1999. Ecosystem metabolism and the global carbon cycle. Trends Ecol. Evol. 14, 249.
Defries, R.S., Field, C.B., Fung, I., Collatz, G.J., Bounoua, L., 1999. Combining satellite data and biogeochemical models to estimate global effects of human-induced land cover change on carbon emissions and primary productivity. Global. Biogeochem. Cy. 13 (3), 803–815.
Dong, T., Liu, J., Qian, B., Zhao, T., Jing, Q., Geng, X., Wang, J., Huffman, T., Shang, J., 2016. Estimating winter wheat biomass by assimilating leaf area index derived from fusion of Landsat-8 and MODIS data. Int. J. Appl. Earth. Obs. 49, 63–74.
Duncker, P.S., Raulundrasmussen, K., Gundersen, P., Katzensteiner, K., 2012. How forest management affects ecosystem services, including timber production and economic return: synergies and trade-offs. Ecol. Soc. 17, 781–784.
Emelyanova, I.V., McVicar, T.R., Van Niel, T.G., Li, L.T., van Dijk, A.I.J.M., 2013. Assessing the accuracy of blending Landsat–MODIS surface reflectances in two landscapes with contrasting spatial and temporal dynamics: a framework for algorithm selection. Remote Sens. Environ. 133, 193–209.
Feng, X., et al., 2007. Net primary productivity of China's terrestrial ecosystems from a process model driven by remote sensing. J. Environ. Manag. 85 (3), 563–573.
Field, C.B., Behrenfeld, M.J., Randerson, J.T., Falkowski, P., 1998. Primary production of the biosphere: integrating terrestrial and oceanic components. Science 281 (5374), 237.
Gao, F., Masek, J., Schwaller, M., Hall, F., 2006. On the blending of the Landsat and MODIS surface reflectance: predicting daily Landsat surface reflectance. Geosci. Remote. IEEE. T. 44, 2207–2218.
Grimm, N.B., Faeth, S.H., Golubiewski, N.E., Redman, C.L., Wu, J., Bai, X., et al., 2008. Global change and the ecology of cities. Science 319 (5864), 756–760.
Guangdong Statistics Bureau, 2001. Guangdong Statistical Yearbook. 2001. China Statistics Press.
Guangdong Statistics Bureau, 2009. Guangdong Statistical Yearbook. 2009. China Statistics Press.
Guangdong Statistics Bureau, 2015. Guangdong Statistical Yearbook. 2015. China Statistics Press.
Hwang, T., Kang, S., Kim, J., Kim, Y., Lee, D., Band, L., 2008. Evaluating drought effect on MODIS Gross Primary Production (GPP) with an eco-hydrological model in the mountainous forest, East Asia. Glob. Chang. Biol. 14, 1–20.
Imhoff, M.L., Bounoua, L., DeFries, R., Lawrence, W.T., Stutzer, D., Tucker, C.J., Ricketts, T., 2004. The consequences of urban land transformation on net primary productivity in the United States. Remote Sens. Environ. 89, 434–443.
Jarihani, Abdollah, McVicar, Tim, Van Niel, Thomas, Emelyanova, Irina, Callow, John, Johansen, Kasper, 2014. Blending Landsat and MODIS data to generate multispectral indices: a comparison of "index-then-blend" and "blend-then-index" approaches. Remote Sens. 6 (10), 9213–9238.
Jiang, C., Wu, Z.F., Cheng, J., Yu, Q., Rao, X.Q., 2015. Impacts of urbanization on net primary productivity in the Pearl River Delta, China. Int. J. Plant Prod. 9.
Jönsson, P., Eklundh, L., 2004. TIMESAT—a program for analyzing time-series of satellite sensor data. Comput. Geosci. 30 (8), 833–845.
Lieth, H., Whittaker, R.H., 1975. Primary Productivity of the Biosphere. vol. 14. Springer Science & Business Media.
Liu, J., Liu, M., Tian, H., Zhuang, D., Zhang, Z., Zhang, W., Tang, X., Deng, X., 2005. Spatial and temporal patterns of China's cropland during 1990–2000: an analysis based on Landsat TM data. Remote Sens. Environ. 98, 442–456.
Liu, X.P., Liang, X., Xu, X.C., Ou, J.P., Li, X., 2017. An Integrated Model for Muti-type Land Use Scenario Simulation by Coupling Human and Natural Effects. Landscape. Urban. Plan.
Lu, D., Xu, X., Tian, H., Moran, E., Zhao, M., Running, S., 2010. The effects of urbanization on net primary productivity in southeastern China. Environ. Manag. 46, 404–410.
Luo, T.X., 1996. Patterns of Net Primary Productivity for Chinese Major Forest Types and Its Mathematical Models. Ph.D. Thesis. Chinese Academy of Sciences, pp. 45–170.
Monteith, J.L., 1972. Solar radiation and productivity in tropical ecosystems. J. Appl. Ecol. 9, 747–766.
Myneni, R.B., et al., 2001. A large carbon sink in the woody biomass of Northern forests. Proc. Natl. Acad. Sci. U. S. A. 98 (26), 14784–14789.
Ni, J., 2003. Net primary productivity in forests of China: scaling-up of national inventory data and comparison with model predictions. For. Ecol. Manag. 176 (1), 485–495.
Nizeyimana, E., Petersen, G.W., Imhoff, M.L., Sinclair, H.R., Waltman, S.W., Reed-Margetan, D.S., Levine, E.R., Russo, J.M., 2001. Assessing the impact of land conversion to urban use on soils with different productivity levels in the USA. Soil Sci. Soc. Am. J. 65, 391–402.
Oke, T.R., Crowther, J.M., Mcnaughton, K.G., Monteith, J.L., Gardiner, B., 1989. The micrometeorology of the urban forest [and discussion]. Phil. Trans. R. Soc. London 324 (1223), 335–349.
Olexa, E.M., Lawrence, R.L., 2014. Performance and effects of land cover type on synthetic surface reflectance data and NDVI estimates for assessment and monitoring of semi-arid rangeland. Int. J. Appl. Earth Obs. Geoinf. 30, 30–41.
Pei, F., Li, X., Liu, X., Wang, S., He, Z., 2013. Assessing the differences in net primary productivity between pre- and post-urban land development in China. Agric. Forest. Meteorol. 171-172, 174–186.
Potter, C.S., Randerson, J.T., Field, C.B., Matson, P.A., Vitousek, P.M., Mooney, H.A., Klooster, S.A., 1993. Terrestrial ecosystem production: a process model based on global satellite and surface data. Global Biogeochem. Cy. 7, 811–841.
Pouyat, R.V., Yesilonis, I.D., Russell-Anelli, J., Neerchal, N.K., 2007. Soil chemical and physical properties that differentiate urban land-use and cover types. Soil Sci. Soc. AMJ 71 (3), 1010–1019.
Prentice, K.C., Fung, I.Y., 1990. The sensitivity of terrestrial carbon storage to climate change. Nature 346, 48–51.
Shenzhen Statistics Bureau, 2015. Shenzhen Statistical Yearbook. 2015. China Statistics Press.
Shochat, E., Warren, P.S., Faeth, S.H., Mcintyre, N.E., Hope, D., 2006. From patterns to emerging processes in mechanistic urban ecology. Trends Ecol. Evol. 21 (4), 186–191.
Singh, D., 2011. Generation and evaluation of gross primary productivity using Landsat data through blending with MODIS data. Int. J. Appl. Earth. Obs. 13, 59–69.
Svirejeva-Hopkins, A., Schellnhuber, H.J., Pomaz, V.L., 2004. Urbanised territories as a specific component of the global carbon cycle. Ecol. Model. 173, 295–312.
Thornthwaite, C.W., 1948. An approach toward a rational classification of climate. Geogr. Rev. 38, 55–89.
Tian, G., Qiao, Z., 2014. Assessing the impact of the urbanization process on net primary productivity in China in 1989–2000. Environ. Pollut. 184, 320–326.
Tian, F., Wang, Y., Fensholt, R., Wang, K., Zhang, L., Huang, Y., 2013. Mapping and evaluation of NDVI trends from synthetic time series obtained by blending Landsat and MODIS data around a coalfield on the loess plateau. Remote Sens. 5, 4255–4279.
Trenberth, K.E., et al., 2007. Observations: surface and atmospheric climate change. Climate Change 2007: The Physical Science Basis. Contribution of Working Group I to the Fourth Assessment Report of the Intergovernmental Panel on Climate Change (Solomon, S. et al., eds). Cambridge University Press, pp. 235–336.
Wang, J.R., Wu, H.J., Sun, X., Li, M.S., Wei, A.S., 2016. Forest carbon storage and dynamic change in Guangdong Province. J. Northeast. Forest. U. 44 (01), 18–22.
Wise, M., Kyle, G.P., Dooley, J.J., Kim, S.H., 2010. The impact of electric passenger transport technology under an economy-wide climate policy in the United States: carbon dioxide emissions, coal use, and carbon dioxide capture and storage. Int. J. Greenh. Gas. Con. 4 (2), 301–308.
Wu, S., Zhou, S., Chen, D., Wei, Z., Dai, L., Li, X., 2014. Determining the contributions of urbanisation and climate change to NPP variations over the last decade in the Yangtze River Delta. China. Sci Total Environ. 472, 397–406.
Xu, C., Liu, M., An, S., Chen, J.M., Yan, P., 2007. Assessing the impact of urbanization on regional net primary productivity in Jiangyin County, China. J. Environ. Manag. 85, 597–606.
Ye, C.S., Dong, Y.X., 2010. Effects of land use change on ecosystem service value of the Pearl River Delta. Trop. Geog. 30 (603-608,621).
Ye, J.S., Yu, G.H., 2010. Forest carbon dynamics in Guangdong Province. J. NANJING. Forest. J. Nanjing. Forest. U (Nat. Sci. Ed) 34 (4), 7–12.
Yu, D.Y., Shao, H.B., Shi, P.J., Zhu, W.Q., Pan, Y.Z., 2009. How does the conversion of land cover to urban use affect net primary productivity? A case study in Shenzhen City, China. Agric. Forest. Meteorol. 149, 2054–2060.
Zhu, X., Chen, J., Gao, F., Chen, X., Masek, J.G., 2010. An enhanced spatial and temporal adaptive reflectance fusion model for complex heterogeneous regions. Remote Sens. Environ. 114, 2610–2623.